Nuclear Instruments and Methods in Physics Research A 827 (2016) 171–180

Contents lists available at ScienceDirect

Nuclear Instruments and Methods in Physics Research A

journal homepage: www.elsevier.com/locate/nima

Particle detection and classification using commercial off the shelf CMOS image sensors

Martín Pérez [a,b,c], Jose Lipovetzky [a,b,c,*], Miguel Sofo Haro [a,c], Iván Sidelnik [a,c], Juan Jerónimo Blostein [a,c], Fabricio Alcalde Bessia [a,c], Mariano Gómez Berisso [a,c]

[a] *Instituto Balseiro, Av. Bustillo 9500, Bariloche, 8400, Argentina*
[b] *Comisión Nacional de Energía Atómica (CNEA), Centro Atómico Bariloche, Av. Bustillo 9500, Bariloche 8400, Argentina*
[c] *Consejo Nacional de Investigaciones Científicas y Técnicas, Centro Atómico Bariloche, Av. Bustillo 9500, 8400 Bariloche, Argentina*

ARTICLE INFO

Article history:
Received 4 November 2015
Received in revised form
6 April 2016
Accepted 17 April 2016
Available online 3 May 2016

Keywords:
Radiation detectors
CMOS image sensors
Alpha Particles
Beta rays
Gamma rays
X-rays
Dosimetry

ABSTRACT

In this paper we analyse the response of two different Commercial Off The shelf CMOS image sensors as particle detectors. Sensors were irradiated using X-ray photons, gamma photons, beta particles and alpha particles from diverse sources. The amount of charge produced by different particles, and the size of the spot registered on the sensor are compared, and analysed by an algorithm to classify them. For a known incident energy spectrum, the employed sensors provide a dose resolution lower than microGray, showing their potentials in radioprotection, area monitoring, or medical applications.

1. Introduction

The detection of ionizing particles has important applications in radioprotection, medical applications, experimental techniques for study of condensed matter, industry, homeland security, environmental monitoring, and subatomic physics. Among different detectors which can be used to detect ionizing particles, image sensors in integrated circuits provide the possibility of having a detector which consumes low power, is much smaller, portable and provides a spatial resolution much better than traditional detectors [1].

Complementary Metal Oxide Semiconductor (CMOS) integrated circuits with Active Pixel Sensors (APS) arrays are widely used in Commercial Off The Shelf (COTS) cameras in consumer electronics, and have usually very low costs, in the range of few dollars, with low power consumptions. This work proposes the use of COTS CMOS image sensors as ionizing particle detectors, with the possibility of partially differentiating the type of incident particle with an analysis of the ionization charge and the pattern recorded by pixels in the image acquired. In this work the possibilities and limitations of such detectors are discussed.

Different works have dealt with the design of specially designed CMOS image sensors for the detection of ionizing particles. References [1–3] present the design and use of a fast APS array specially designed for the ALICE experiment at CERN, which uses correlated double sampling for the on-pixel correction of the Fixed Pattern Noise (FPN) caused by transistor mismatch along the array. Reference [4] shows the Medipix2 chip, a readout pixel chip specially designed for charge particle detection using arrays of different detectors being able of providing 100% fill factor. The readout of each pixel comprises a preamplifier, a discriminator, and a register, which requires 504 transistor inside each cell. The complexity of the sensors allows a high temporal resolution and suppression of FPN.

Furthermore, reference [5] describes a detector array built in a high voltage power CMOS process which allows applying very high voltages to create deep depletion areas which allow the collection of more charge and have a 100% fill factor. Reference [6] presents the design and fabrication of a detector named MIMOSA (Minimum Ionising particle MOS Active pixel sensor) which uses a thin depleted epitaxial layer to improve the charge collection. Works [7] and [8] present an improved version of the detector developed with the aim of detecting thermal and fast neutrons. Thermal neutrons are detected using a boron conversion layer, and energetic neutrons with use a plastic converter, but results were

---

[*] Corresponding author at: Centro Atómico Bariloche, Av. Bustillo 9500, Bariloche, 8400, Argentina.
E-mail address: lipo@cab.cnea.gov.ar (J. Lipovetzky).

http://dx.doi.org/10.1016/j.nima.2016.04.072
0168-9002/

not presented in that work. Later, the same group presented a thinned chip to be able to detect the alpha particles [9] generated in the boron conversion layer. Besides, in a recent work it is shown that thermal and epithermal neutrons can be detected with high spatial resolution by coating a Charge Couple Devices (CCD) sensor with a boron conversion layer [10]. All these works used chips fabricated specially for the detection of charged particles.

On the other hand, only few works have dealt with the use of COTS sensors as charged particle detectors. In [11] the response of COTS CMOS imagers as ionizing radiation detectors in the detection of X-ray photons is studied. Then, the same group presents in [12] the response of two COTS chips and studies its potential use in interventional radiology dosimetry and for the detection of protons and location of the proton hit [13,14]. In [15], the use of cell phones cameras to detect shower of particles from cosmic rays is proposed, and the response of the sensor to different sources is compared. A system comprising a world-wide array of cell phones running a dedicated app would have a large effective section and allow local monitoring of radiation levels.

This work studies the response of two COTS CMOS imager sensors to different kinds of incident radiation; including beta particles, gamma photons, X-ray photons, and alpha particles; showing the possibility of partially identifying the type of incident particle through the pattern in the image and deposited charge. The image sensors used are embedded in low cost cameras, showing the possibility of, with adequate processing, the development of inexpensive detectors for wide applications, area monitoring, radioprotection, dosimetry during imaging interventions or other medical applications. The aim of the work is to show the feasibility of using such a device at room temperature.

The use of COTS sensors brings in several applications important advantages with respect to integrated circuits designed ad hoc for a specific application. The first and obvious advantage is the low cost of each sensor. The sensors used in this work have costs in the order of few US dollars, which would allow the manufacture of low cost personal dosimeters for the protection of workers in radiation facilities and medical image facilities not only in developed countries but also in the third world. Low cost allows the integration at an affordable price of arrays of detectors, for example to build an array for the characterization of radiotherapy shaped fields. Other possible application is the construction of a macroscopic linear array of these sensors to measure the angular dependency of the diffracted particles in diffraction experiments. Another important advantage is that COTS sensors are available in the market and can be easily purchased and delivered, and are well-documented, whereas experimental Application Specific Integrated Circuits (ASICs) designed for harsh environments are more difficult or impossible to obtain due for example to ITAR regulations. For that reason, there is a tendency to try to use whenever possible COTS circuits for space applications [16–18], including different CMOS and CCD COTS image sensors [19–21].

Another advantage of COTS cameras is that since the technology pushes to produce sensors with a higher number of pixels in comparable sensitive areas, the pixel size and thus spatial resolution improves faster than ad hoc designed ASICs. For example the color sensor used in this paper has a pixel lateral size at least three times smaller than [7–9,5]. On the other hand, the use of COTS sensors will have limitations compared to ad hoc ASIC, for example time resolution, low noise, or total dose response [5,9,10] which might be important for other applications.

Next section presents the devices used in this work, and the algorithm used for FPN suppression. Section 3 shows the response of the sensors to different kinds of radiation from different sources, and some characteristics of the patterns obtained in the images with the different particles. Section 4 shows the sensors used as particle counters in a real application; and an algorithm to distinguish between alpha and gamma events. Section 5 presents the conclusions of the work.

2. Devices under test and image processing

This section describes the COTS devices used in this work, and the image processing strategy used to discern between different incident particles using these devices.

2.1. Image sensors used in this work

Two commercial cameras based on CMOS APS sensor arrays were used in this work. The cameras are CGH 309D and JMK JK-801. The first camera is based on the APTINA MT9V011 0.25 color CMOS sensor, 640×480 pixels with a size of $5.6\ \mu m \times 5.6\ \mu m$, which has a RGB Bayer pattern filter applied. The second camera is based on the OmniVision OV5116N black and white (BW) CMOS sensor, 320×240 pixels of $11\ \mu m \times 11\ \mu m$. The sensor does not have a color filter on it, as will be shown later. The cameras comprise an image processing circuit, the ViMicro VC0702, which provides a PAL-N video signal which was captured using a USB grabber that digitalizes the signal using 8 bits. Fig. 1 shows pictures of the devices used in this work.

The structure of the sensors was analysed using a Focus Ion Beam (FIB) and a Scanning Electron Microscope (SEM) to study the thickness of the layers placed on the active silicon area [22]. The BW sensor has an oxide layer with a thickness of $\simeq 2.7\ \mu m$ on top of the silicon epitaxial layer, which is the active volume of the sensor. Most of each pixel is covered only with this oxide layer, and a fraction of its area with metal paths embedded in the oxide. The color sensor has a Bayer filter with thicknesses from $\simeq 4\ \mu m$ to $\simeq 5\ \mu m$, and then an oxide layer of $\simeq 4\ \mu m$ on top of the silicon. Incoming particles, or particles produced by the incident radiation after some interaction, will need to penetrate these layers to reach the active silicon volume.

As a normalization and to allow a simpler comparison of the results of both sensors, the results obtained in the color sensor are the average of the three colors, which lead to an equivalent pixel pitch of $11\ \mu m \times\ 11\ \mu m$.

All measurements were done acquiring thirty images per second and storing them for their analysis. During our experiments, the sensors were integrating charge almost all the time of the period.

2.2. FPN suppression

Since our aim is to use these COTS image sensors at room temperature for the detection of charged particles, several efforts had to be done in order to mitigate some unwanted effects.

One of these unwanted effect which, as will be seen later, needs

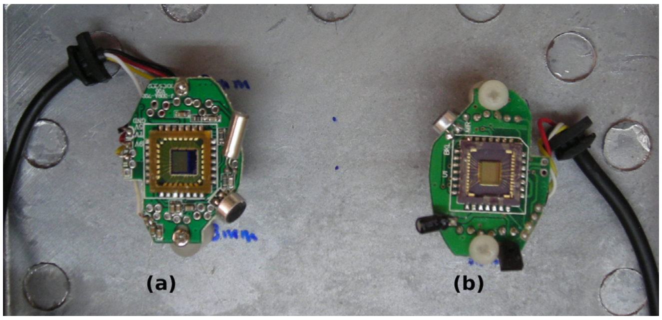

Fig. 1. Board with (a) color sensor CGH 309D, and (b) with black and white sensor MK JK-801.

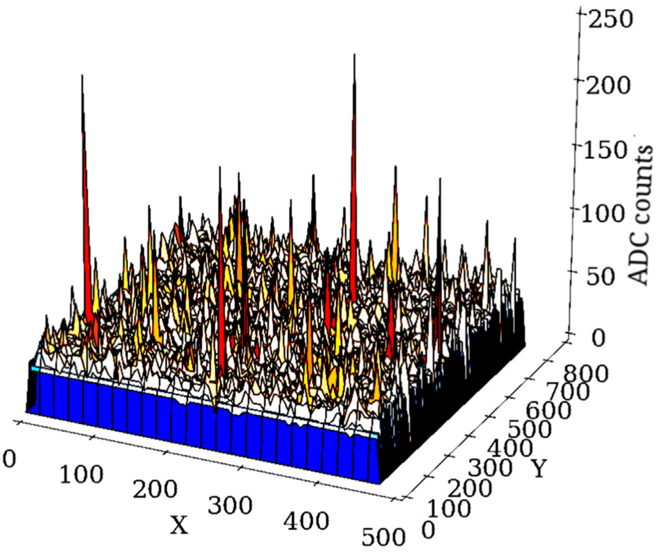

Fig. 2. Dark image mesh without FPN suppression.

to be minimized, is the reduction of random dark noise and defective pixels which leads to a FPN—that also has a random component which depends on each pixel of the employed sensor. Fig. 2 presents the values of the ionization charge recorded on the color image sensor blacked out and without incident particles. The readings of most pixels have a small but not null value. Also, a small number of pixels have very high readings, with values notoriously higher than the average of the whole image. Moreover, the readings of pixels in dark conditions have a slow time dependence. These values are probably not only the result of pixels with defects, it can also be improper zeroing along the several amplifying and conversion stages [22]. Similar results were obtained with the BW sensor.

The mean value of FPN showed to be temperature dependent. The statistical distribution of values read in the dark images is plotted in Figs. 3 and 4. The read values in all the pixels in 36,000 frames were arranged in recorded histograms, in the curves referred to as "no filter". The measurements were done at 20 °C and 40 °C to illustrate the effect of temperature. At both temperatures most of the readings yield low values, in normal operating conditions, but a very small proportion of the pixels yield values quite higher. These pixels with high values correspond to the spikes in Fig. 2.

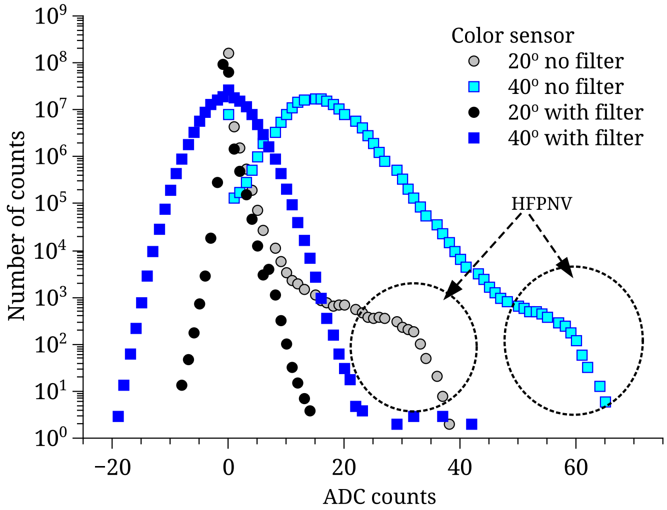

Fig. 3. Histogram of the ionization charge recorded in the color sensor in dark conditions. The original values are compared with the result of applying the filter to reduce FPN.

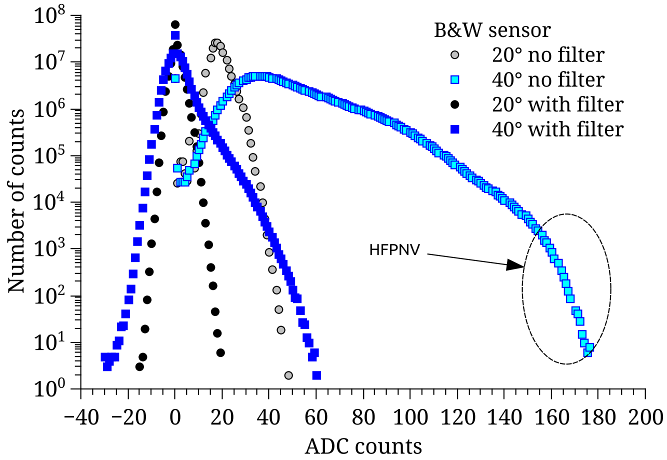

Fig. 4. Histogram of the ionization charge recorded in the BW sensor in dark conditions. The original values are compared with the result of applying the filter to reduce FPN.

Since our strategy to detect a particle will be to localize events in which the value read in a cluster of pixels is higher than a threshold, it is necessary to eliminate this average FPN, specially the values with High Fixed Pattern Noise Values (HFPNV) presented in the figures. To reduce the impact of FPN on the detection of ionizing particles, we subtract the mean value of FPN to each image. Since this mean value might slowly change with time, we used a one tap autoregressive filter of order 1, with a time constant of 128 images, which has a low computational cost and can be easily implemented in an Field Programmable Gate Array (FPGA) or a microprocessor or microcontroller in a future stand-alone version of an instrument.

If we treat each frame as a matrix, with $I_{READ}(n)$ being the frame read at time n, the average FPN matrix $I_{FPN}(n)$ is computed using Eq. (1) with $a = 1/128$. The clean image after noise suppression $I_{CLEAN(n)}$ is obtained with Eq. (2).

$$I_{FPN}(n) = I_{FPN}(n-1)\cdot(1-a) + I_{READ}(n)\cdot a \tag{1}$$

$$I_{CLEAN}(n) = I_{READ}(n) - I_{FPN}(n) \tag{2}$$

Figs. 3 and 4 show histograms of the values of several consecutive images before fixed pattern suppression I_{READ} and after fixed pattern suppression I_{CLEAN} for the color sensor and BW sensor respectively. Figs. 3 and 4 show that even for the operation at 40 °C the number of pixels over 20 and 60 ADC counts is negligible.

Another problem which might appear would be the auto-gain feature of some image sensors. In our experiments the almost constant mean value of dark noise and FPN ensure that the gain is kept constant along the experiments. Also, care should be taken disabling the interleaving sometimes used by image acquisition software.

It will be shown in the next section that the pattern left by the incident charged particles employed in this work is formed by a cluster of pixels with values much higher than the remaining random noise after the FPN mitigation. Thus, it is possible to assume that a group of adjacent pixels with values over a given threshold are the detection of a particle and not random noise, yielding a negligible rate of false positives.

3. Response to different particles

This section presents the response of the sensors mentioned in

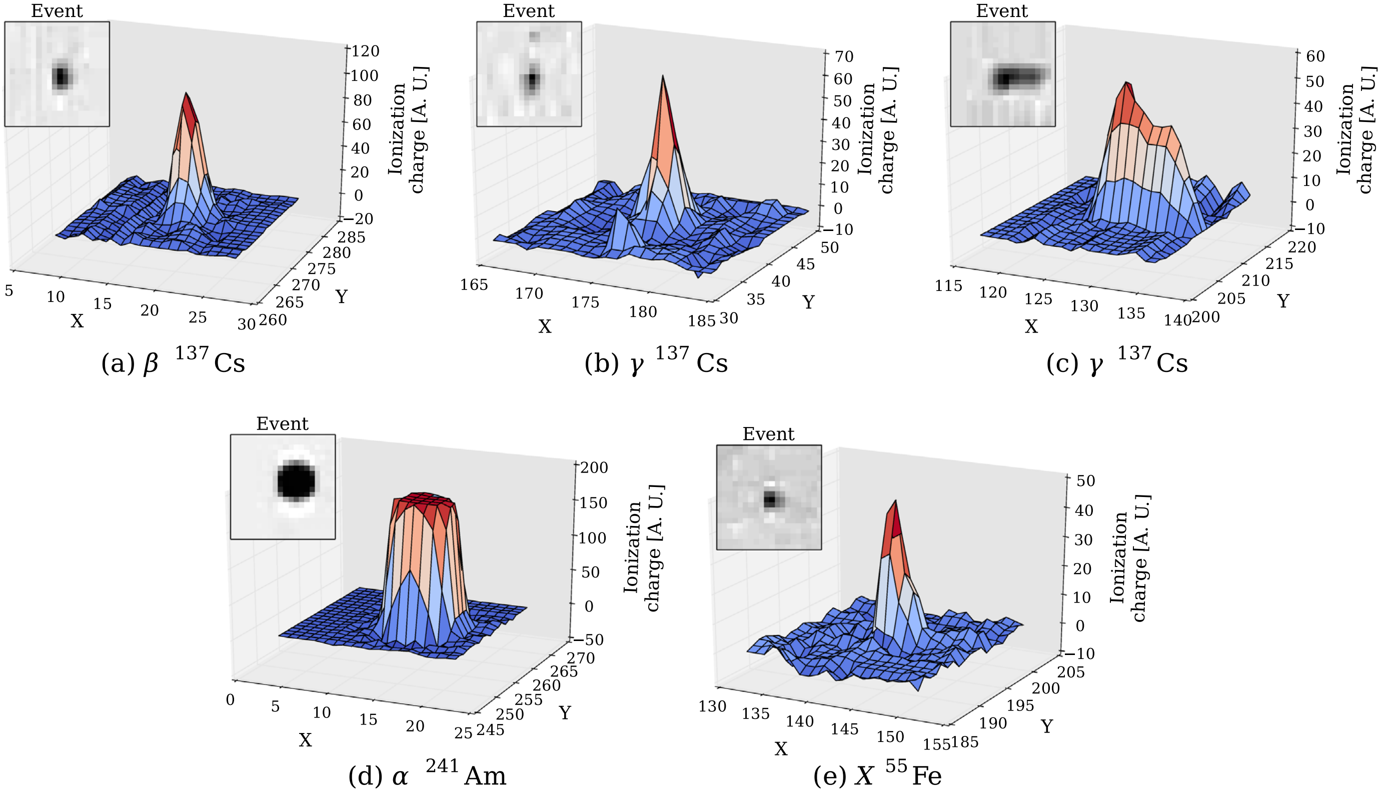

(a) β ^{137}Cs (b) γ ^{137}Cs (c) γ ^{137}Cs

(d) α ^{241}Am (e) X ^{55}Fe

Fig. 5. Mesh of typical events with alpha, beta, gamma, X-ray in color sensor.

Section 2 to the irradiation with different charged particles and photons. All the plots and analysis presented in this section are from data processed with the FPN suppression presented in last section. Thus, the values obtained will be named ionization charge and presented in the arbitrary units of an ADC count. Unless otherwise is specified, all measurements were done using a distance between the sources and the sensor smaller than 2 cm.

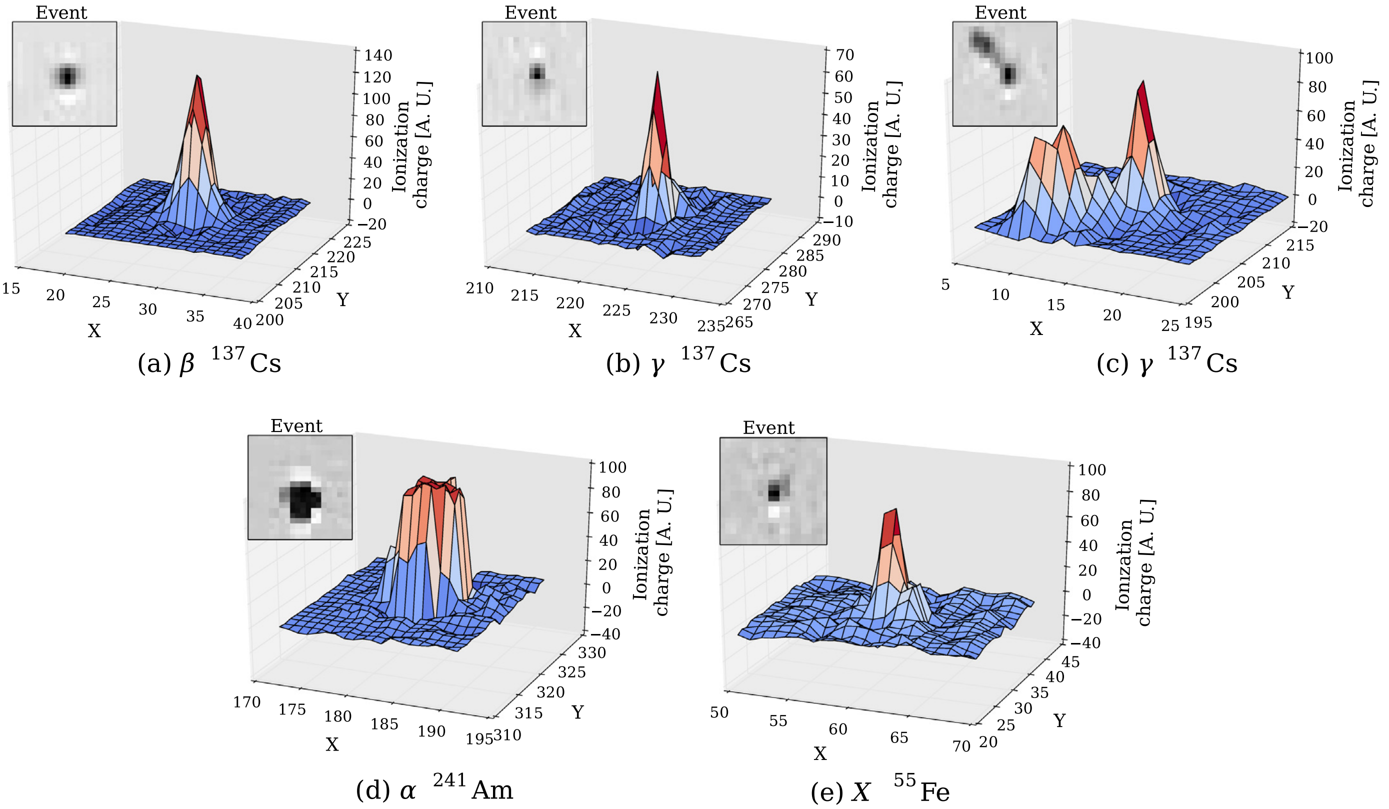

(a) β ^{137}Cs (b) γ ^{137}Cs (c) γ ^{137}Cs

(d) α ^{241}Am (e) X ^{55}Fe

Fig. 6. Mesh of typical events with alpha, beta, gamma, X-ray photon in BW.

3.1. Typical event responses

The image sensors were exposed to different radioactive sources which emit X-rays, gamma rays, alpha and beta particles. The interaction of particles with the sensor produces signal in a small cluster of pixels on the read image. This section presents typical responses obtained with the different particles. Before irradiation, a thin glass window which covers the image sensors was removed, to allow the direct exposure of the sensors to the particles.

When a ionizing particle interacts with the sensor it loses energy generating ionization charge on a cluster of pixels, which can be observed as an illuminated region in the image. Figs. 5 and 6 show typical patterns left by different particles on the color and BW sensor, respectively. The plots show a mesh of the values of a set of pixels around an event, and in the insets the corresponding of the image with the events.

3.1.1. Beta and gamma rays from a ^{137}Cs source

The image sensors were placed at ≃5 mm from a ^{137}Cs source which emits beta particles of 0.514 MeV and 1.174 MeV and photons of 0.662 MeV [23].

Since the attenuation range in Si of the gammas emitted by ^{137}Cs is ≃3.7 cm, much higher than the thickness of the active area of the sensor, only a very small fraction of the incident gamma photons will produce interactions with the active volume of the sensor [8,24]. On the other hand, since the air distance between the source and the detector is sufficiently small, most of the incident betas will interact with the detector. This is because they are charged particles, and its range is higher than the thickness of the insulating layers and active volume of the sensors. Since one beta particle and one gamma particle are emitted in each beta decay, most of the observed events in this experiment are beta particles. Typical patterns left in the sensors by these particles are shown in Figs. 5a and 6a.

In order to check the nature of the radiation detected, a 5 mm sheet of acrylic was placed between the source and the detectors, and the experiment was repeated. This sheet is thick enough to stop all beta particles from the source [25]. However, since it is much thinner than the mean free path of the gamma rays, almost all the photons could pass this sheet, as was experimentally verified using a NaI(IT) scintillator [22].

Then, the experiment was repeated with this configuration in which the beta particles from the source are stopped, and only gamma photons—or electrons generated by the bremsstrahlung photons produced by beta particles—photoelectric and Compton effects are expected. Figs. 5b and c and 6b and c show typical patterns observed in the sensor with this configuration. The patterns recorded by the sensor were not only dots, but also small traces. The reason of these different patterns is that gamma rays from ^{137}Cs interact with silicon mainly by Compton Effect [26], thus generating Compton electrons leaving with different directions. The dots can be understood as electrons scattered into the sensors in a normal direction, whereas traces can be caused by electrons hitting the sensors with grazing angles.

3.1.2. Beta particles from a ^{152}Eu source

The sensors were exposed to 356 keV beta particles and gamma ray with energies below 1408 keV from a ^{152}Eu source [23]. The results are analysed below, but the patterns were similar to what was shown for ^{137}Cs in both kinds of sensors and are not displayed here.

3.1.3. Gamma rays from ^{60}Co, ^{133}Ba, sources

The sources were encapsulated, and the emitted beta particles could not leave the source. The same experiment was repeated using a ^{60}Co source which emits gamma rays with energies of 1.173 MeV and 1.332 MeV [23], and a ^{133}Ba shielded source which emits gamma photons below 383.9 keV [23]. The patterns were similar to what was obtained with gamma photons from ^{137}Cs and are not displayed here.

3.1.4. X-ray irradiation from a ^{55}Fe source

The experiment was repeated with a ^{55}Fe source, which emits X-ray with energies of 5.9 and 6.5 keV, which have attenuation lengths of 28 μm and 38 μm in Silicon [24], most of them being absorbed in the active region of the sensors. Typical responses are plotted in Figs. 5e and 6e.

3.1.5. Alpha particles and photons from ^{241}Am and ^{235}U Sources

The experiment was repeated using two ^{241}Am sources. The isotope ^{241}Am emits alpha particles with energies of ≃4.4 MeV and X-ray up to 60 keV [23]. One of the sources has a shielding which stops alpha particles, whereas the other source has only a very thin protection layer, allowing the emission of both types of particles. The first source will be referred to as *shielded ^{241}Am source* and the second as *unshielded ^{241}Am source*.

The distance between the source and sensors was less than 5 mm, ensuring that alpha particles would not be stopped by air. With the unshielded source two different groups of patterns were observed, a first group similar to the patterns observed with X-rays, and also a group of patterns generally bigger and in which the reading of the sensor was saturated. As an example, Figs. 5d and 6d show these different patterns that we associate to alpha particles.

The same experiment was carried out using a natural uranium source, which emits alpha particles with 4.679 MeV and photons. The spots observed in the image were similar to what was observed for ^{241}Am.

3.2. Charge collected after different events

Long irradiations were carried out using each source, with the aim of collecting high numbers of events. The videos obtained were processed applying the FPN suppression algorithm and then each event was detected. For each event, we summed the ionization charge collected in all the pixels of the cluster, considering a cluster as a 10×10 pixel box in the image, centered in the pixel with the maximum value of each event. This sum is proportional to all the charge trapped in the active volume of the detector after each event, i.e. a measure in the arbitrary units of the ADC of all the collected charge. A large number of events were recorded for each source and particle, and the number of events detected vs. the amount of charge—in a.u.—are shown in the histograms of Figs. 7 and 8 for color and BN cameras, respectively. Each figure has three subplots. The subplot on the top shows the histograms from ^{241}Am and ^{235}U photon and alpha sources. The subplots on the middle and bottom show the histograms with the other sources which emit betas, gamma photons, or X-ray. The histograms show that despite the differences in energies, the charge collected from photons and electrons has so much dispersion that it is difficult to find differences among the curves. However, a clear difference is observed when alpha particles interact with the detector, clusters with a quite higher amount of charge are detected. This becomes clear comparing the curves for ^{241}Am with and without shielding, i.e. without and with alpha particles, respectively. Particularly, in Fig. 8 a high number of events with charge from 1500 to 3500 a.u. are observed for the unshielded source. These events do not occur with the shielded source. For the color cameras, which use a Bayer Filter, it can be seen that there is a high number of events with charges higher than 3000 a.u. clearly not observed when the irradiation is carried out with shielded sources. These events which leave higher levels of charge in the pixels can

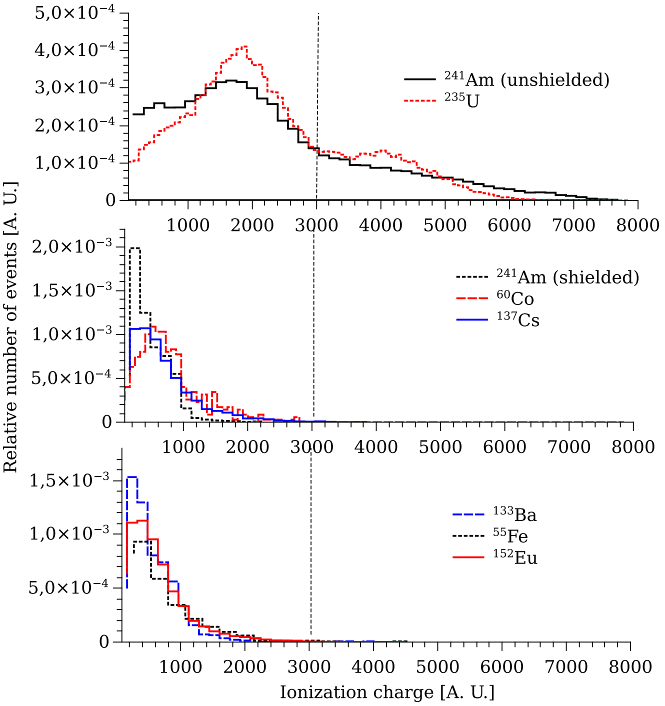

Fig. 7. Histograms of charge (in a.u) produced by particles from different sources for color sensor.

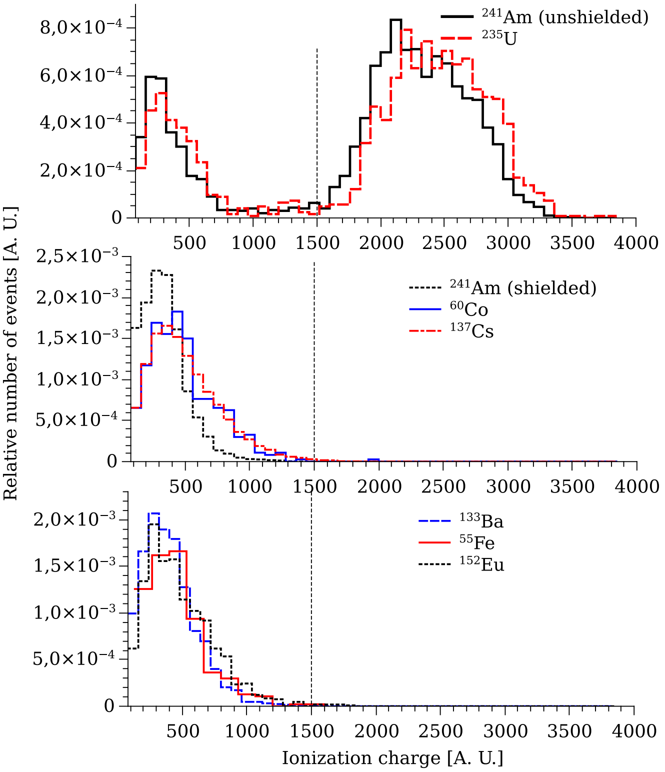

Fig. 8. Histograms of charge (in a.u) produced by particles from different sources for BW sensor.

be associated to alpha particles, which have a higher Linear Energy Transfer (LET). A comparison of the peaks from Figs. 7 and 8 suggests that the interaction of alpha particles with the Bayer filter might modify the amount of charge collected by the sensor.

Considering that in silicon an average of 3.6 eV are required to create an electron–hole pair, every incoming photon of 6.5 keV from ^{55}Fe will generate ≃1800 pairs. If the photon is absorbed close to the depletion regions a high fraction of the charge is collected by the reversed biased junctions of the pixels. This charge trapped in a set of neighbor pixels leads to the charge in the histograms of Figs. 7 and 8. In the color sensor, the charge after absorbing a photon has a peak in 500 ADC counts, whereas the BW sensor has a peak in 250 counts.

On the other hand, beta particles from ^{137}Cs have 0.514 MeV and 1.176 MeV, much more energy than ^{55}Fe X-rays. However, it can be observed in Figs. 7 and 8 that the amount of charge left in each event is almost the same than for X-rays.

High energy beta particles from ^{137}Cs have a LET from 1.5 to 1.6 MeV cm^2/g, at least ten times lower than the LET of the lower energy photoelectric electrons generated by absorption of ^{55}Fe X-rays. With that LET the beta particles can generate ≃100 pairs/μm. This means that beta particles generate in a distance of ≃18 μm the same amount of charge as an X-ray photon. This distance is comparable to the thickness of epitaxial layers in bulk CMOS processes, and it was reported that in such a depth is where most of the generated charge after a single event is collected [27].

On the other hand, in Figs. 7 and 8 it is clear that the charge left by alpha particles is higher than beta particles or electrons, a result which can be explained by the different LET of the particles. However, since the reading of the pixels in the spots generated by alpha particles correspond to saturation values—probably of the internal preamplifiers—, a linear quantitative comparison cannot be done.

3.3. *Event spot size*

X-ray photons from ^{55}Fe have energies of 5.9 and 6.5 keV [23]. The interaction of these photons with silicon will thus generate mainly photoelectric electrons with energies below 6.5 keV, with a range in silicon—for the electrons—lower than 2 μm [25], smaller than a pixel size. In case a secondary photoelectric photon is emitted from silicon, its energy would be 1.7 keV, with a attenuation length of ≃11 μm [28], to then generate another electron with a short range. This means that most of the times all the charge generated by the absorption of an X-ray photon should be collected within a region smaller than or comparable to the lateral size of a pixel.

However, as was shown in Figs. 5 and 6 the charge deposited after an event is spread in a cluster of several pixels. To illustrate this, Fig. 9 shows an histogram of the radius of events observed in the both sensors using the ^{55}Fe source. These radii were calculated as the second order momentum of the distribution of charge. It can be concluded that despite the fact that the charge left by a photon is supposed to be generated in a volume smaller than a pixel, this charge is usually spread in several pixels, in areas of 100–200 μm^2. Similar spot sizes were observed for X-ray photons in CMOS image sensors with 5.6 μm pixel pitch [11,13].

This result can be explained with the following facts. ^{55}Fe photons have attenuation lengths of 28 and 38 μm, whereas the depletion region of the PN junction in CMOS pixels are usually at a depth lower than 1 μm from the silicon-oxide interface. This means that most of the photons absorbed in the silicon will be absorbed in the bulk of the chip, below the depletion region of the reversed biased junction of the pixel. When the photon is absorbed, it generates in a region of few μm electron–hole pairs, as was stated before. This charge, generated below one pixel, will spread to neighboring pixels by diffusion, leaving the observed spot. This effect is known to cause crosstalk in image sensors when irradiated with visible light [29–31].

The spot size of events generated by alpha particles is slightly bigger, with radius ranging from 33 to 44 μm. Similar results have been reported in CCD image sensors by [32], where the radius of

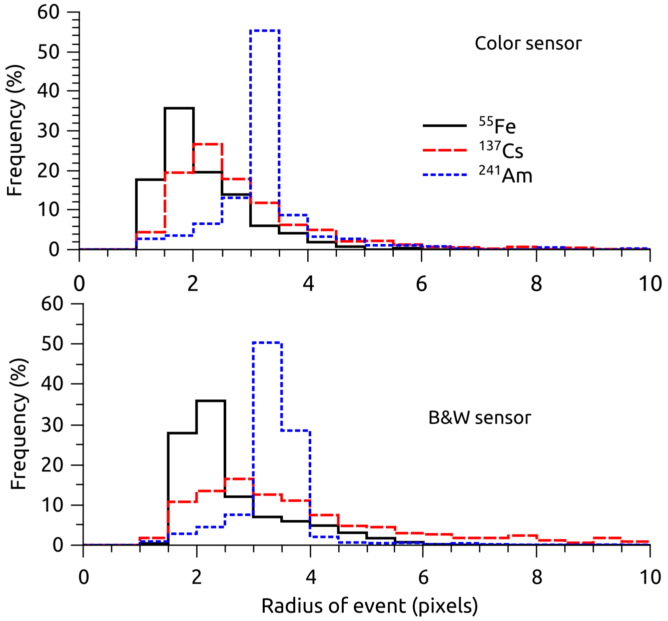

Fig. 9. Radius in pixels. This radius is calculated as the second order momentum of the charge generated during an event.

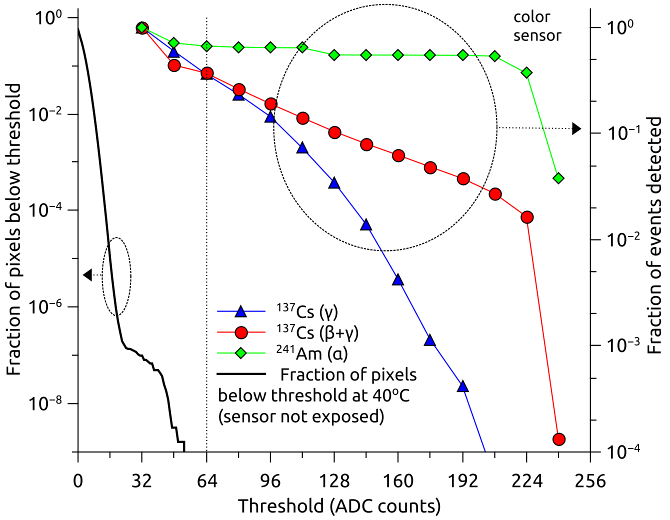

Fig. 10. Determination of a threshold to improve sensitivity. Referenced to the left vertical axis, the fraction of pixels with values lower than each threshold is plotted. The data is obtained from a color sensor at 40°. Referenced to the right vertical axis, the relative number of events which have a maximum over each threshold is shown.

the alpha events for similar energies is approximately two pixels. The pitch between pixels is 15 μm, yielding a radius of ≃30 μm.

4. Discussion and applications

This section discusses possible applications of the sensors and their performance as particle counters.

4.1. Particle counting, sensitivity and threshold dependency

A detector using these sensors would count the arrival of a particle whenever, after FPN suppression, a set of pixels has intensity values higher than a threshold. If this threshold is chosen too low, the random values of dark noise would lead to false counts. On the other hand, if the threshold is too high, many events will be ignored, leading to a low responsivity and low dose resolution of the system. A good choice for the threshold should consider the trade-off between a extremely low chance of having false counts and do not miss too many events. This trade-off is exemplified in Fig. 10. The solid line, referenced to the left vertical axis, shows the fraction of pixels with values lower than a threshold—horizontal axis—, obtained from the curve at 40 °C after FPN suppression in Fig. 3. This line can be interpreted as an estimation of the probability that randomly chosen pixel in an image has been considered as an event vs. the threshold.

Referenced to the right vertical axes, we plot the number of events detected by the systems in several irradiations when different thresholds are used. The number of events for each threshold is normalized to the number of events using 32 as threshold, to allow a comparison of the different irradiations. Three curves are plotted, the response with alpha particles, gamma photonsfrom ^{137}Cs, and beta and gamma particles from ^{137}Cs. The number of detected particles strongly depends on the threshold used, specially for gamma irradiation, with almost eight orders of magnitude of events counted when the threshold is varied from 32 to 192. To make easier the comparison, the number of events detected with each threshold is normalized to the number of events with a threshold of 32.

To maintain negligible the chance of having a false positive, with a reasonable probability of considering as real an event, we choose to use for this color sensor, a threshold of 64, and decide that an event was detected whenever at least two contiguous points have values over this threshold.

With this consideration, me made an irradiation with a calibrated ^{137}Cs gamma source to estimate the dose resolution of a dosimetry system based on this sensor, considering that a measure of the dose resolution is one count. The sensor was placed at a distance of 29 cm from the source. In that position the dose rate was 1.7 mGy/h, measured with a calibrated detector, valued which agreed with the original calibration of the source considering its decay. At that distance using a threshold of 64 the number of events per second was 9.9, meaning that each event represents ≃50 nGy. This dose per count of course will depend on the photon energy—for gamma irradiation—, or type of incoming particle.

4.2. Sensor as gamma counter at different fluxes

To study the ability of counting particles at different dose rates, and show the system can be used in a real application, the color sensor was exposed to radiation available at the Neutron Imaging Facility, RA6 nuclear research reactor, Bariloche, Argentina [33]. The Neutron Imaging Facility has a radial extraction tube from the reactor core that provides a beam formed by gammas with a wide range of energies, and thermal and epithermal neutrons that for this measurements were attenuated using a polyboron layer.

The measurement consisted in counting the number of events per unit time during the start-up procedure of the RA6 reactor [22]. During start-up, the power of the core was increased from zero to ≃1.5 kW, 10 kW, 30 kW, and 100 kW. The sensor was placed in a dark plastic box with its surface normal to the radiation field. Using the steps proposed—i.e. applying the FPN-mitigation filter and detecting groups of contiguous pixels with values higher than a threshold of 64—, the events were identified in the images, integrating the number of events in 15 s to calculate the average number of counts per frame (ACPF) during the measurement.

Fig. 11 presents the ACPF measured during the experiment. In more detail, the inset of the figure shows the average number of cps vs the reactor power during each power step. The number of cps observed is proportional to the power of the reactor.

The gamma dose rate when the reactor operated at 100 kW

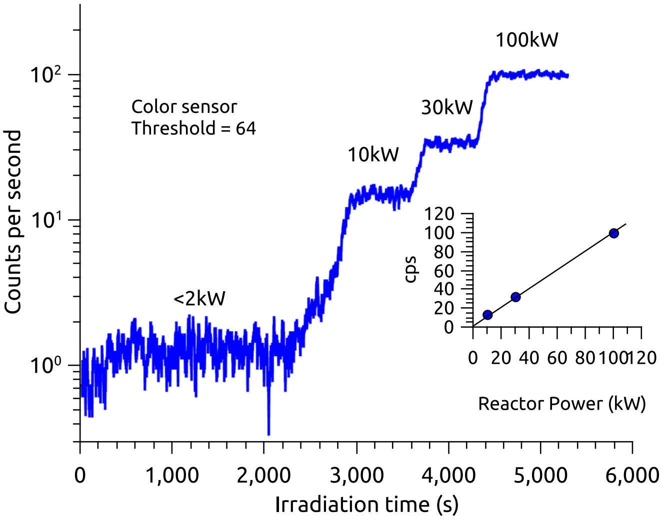

Fig. 11. ACPS during startup reactor RA6.

was ≃160 mGy per hour, estimated from a previous characterization of the facility. At 100 kW the system detected ≃100 counts per second, meaning that each count represents ≃460 nGy. The different sensitivity compared to ^{137}Cs is caused by the different energy spectrum of gamma photons with much higher and different energies [15]. This shows that as happens with many particle counters, the conversion from counts to dose should take into account the photon energy.

4.3. Particle classification

One of the aims of this work is to evaluate the capability of the employed low cost sensors to identify the incoming particle; as was done with CCD sensors in [32,34], where the amount of charge or geometrical features of the event-induced clusters are used. Several characteristics of the spots generated by the trapping of different events were studied in Section 3. Figs. 7 and 8 compare the charge left by different particles, and Fig. 9 compares the radius of the spots. In the three plots it can be concluded that the patterns recorded by photons from few keV to more than one MeV or beta electrons with energies from hundreds of keVs to more than one MeV cannot be distinguished, as was discussed before. However, alpha particles leave different characteristics, a higher amount of charge— Figs. 7 and 8—, different radius— Fig. 9—, and generally higher maximum values read on the pattern—closer to saturation as is observed in Figs. 5 and 6.

We used these differences in the patterns to make an algorithm to identify which particle was detected, based on the charge, radius, and highest pixel value read inside the cluster. Every time an event is detected in the color camera, it is counted as an alpha particle if the total charge is greater than 3000, the radius is higher than 2.5 pixels, and the highest pixel value read in the cluster is higher than 125 a.u.

To prove the concept we made the following experiment. At the facility described in the previous section, we placed in operation and tested the color sensor and a ^{241}Am source was placed next to the sensor. In this preliminary experiment the signal of interest is the alpha particles, and the gammas produced by the RA6 reactor are used as background. A fraction of the active area of the image sensor was covered by a paper sheet with a thickness of ≃100 μm, which is enough to ensure that all alpha particles would be stopped [24]. Fig. 12a shows the shadow caused by the sheet of paper when the sensor is illuminated with a point-like light source placed at several meters from the sensor, showing which part of the sensor was covered.

Fig. 12 shows images under the three irradiation conditions which include all the events registered in 2000 frames—i.e. 66 s. The images on the left show all the events recorded, whereas the images on the right show all the events identified as alpha particles with the algorithm. The images (b) and (c) show the events captured using the ^{241}Am irradiation. All the events are recorded on the uncovered region of the sensor as expected. The total number of events detected was 138, being 101 of them detected as alpha particles—the 37 remaining events do not comply with the classification criterion, meaning that the algorithm has a high false negative rate of about 40%. When the sensor was irradiated with gamma photons the images (d) and (e) were obtained. The events were uniformly distributed along the sensor, a result expected since the thin paper sheet is almost transparent to gamma rays. The total number of events recorded was 9842, and the algorithm identifies 42 false positives, i.e. approximately a 0.4% of gamma photons wrongly identified as alpha particles. When the sensor was exposed to gamma photons and to the ^{241}Am source, the images (f) and (g) were obtained. The total number of events was 9782, with 147 of them identified as alpha particles. The number of events is the sum of the real number of alpha particles and gamma photons mistakenly classified, and is approximately the sum of figures (c) and (e). With the limitations of having ≃0.4% of false positives—gamma photons identified as alpha particles—, the algorithm shows that it is possible to make a particle classification in a mixed field beam composed of particles with quite different LETs. The parameters set in the algorithm were optimized to have a low false positive rate at the cost of having a high false negative rate. This would be useful for example to detect alpha particles from ^{10}B in an application as presented in [7,8] and [10].

The difficulty in separating beta particles from gamma photons at a pixel level is caused by the fact that the particle which is really detected in the thin active layer of the sensors during gamma irradiation is the Compton electron and not the photon itself. In both cases, Compton electrons and Beta particles are electrons with comparable high energies which depend on the emission direction and track. The only way of differentiating them with these devices is through the use of shielding layers as was shown in our experiments. The amount of charge left in the thin epitaxial active layer of the sensors makes difficult also a classification between high and low energy photons.

5. Conclusion

This paper investigated the response of two COTS CMOS sensors embedded in low cost cameras as single particle detectors, showing their potentials and limitations. Through a simple filtering algorithm the temperatures-dependent FPN and dark currents can be reduced, allowing the detection of particles. The response of the sensors to different beta, gamma, X-ray, and alpha sources was obtained, studying the charge collected after each event, the maximum value, and the spot radius. The results show that it is possible to discriminate between events generated by alpha particles and events generated by the other particles used in this work.

Also it was shown that the sensor could be used to count events at different dose rates in a real application. The dose resolution of the detector, which depends on the photon energy, can be set below 1 μGy, with a negligible number of false positives. This result shows that these sensors have potential applications in radioprotection or area monitoring, as well as in medical applications as was reported by [12], under low dose irradiation conditions as used in our work.

The results presented in this work with two different sensors from different vendors, under nine different irradiation sources

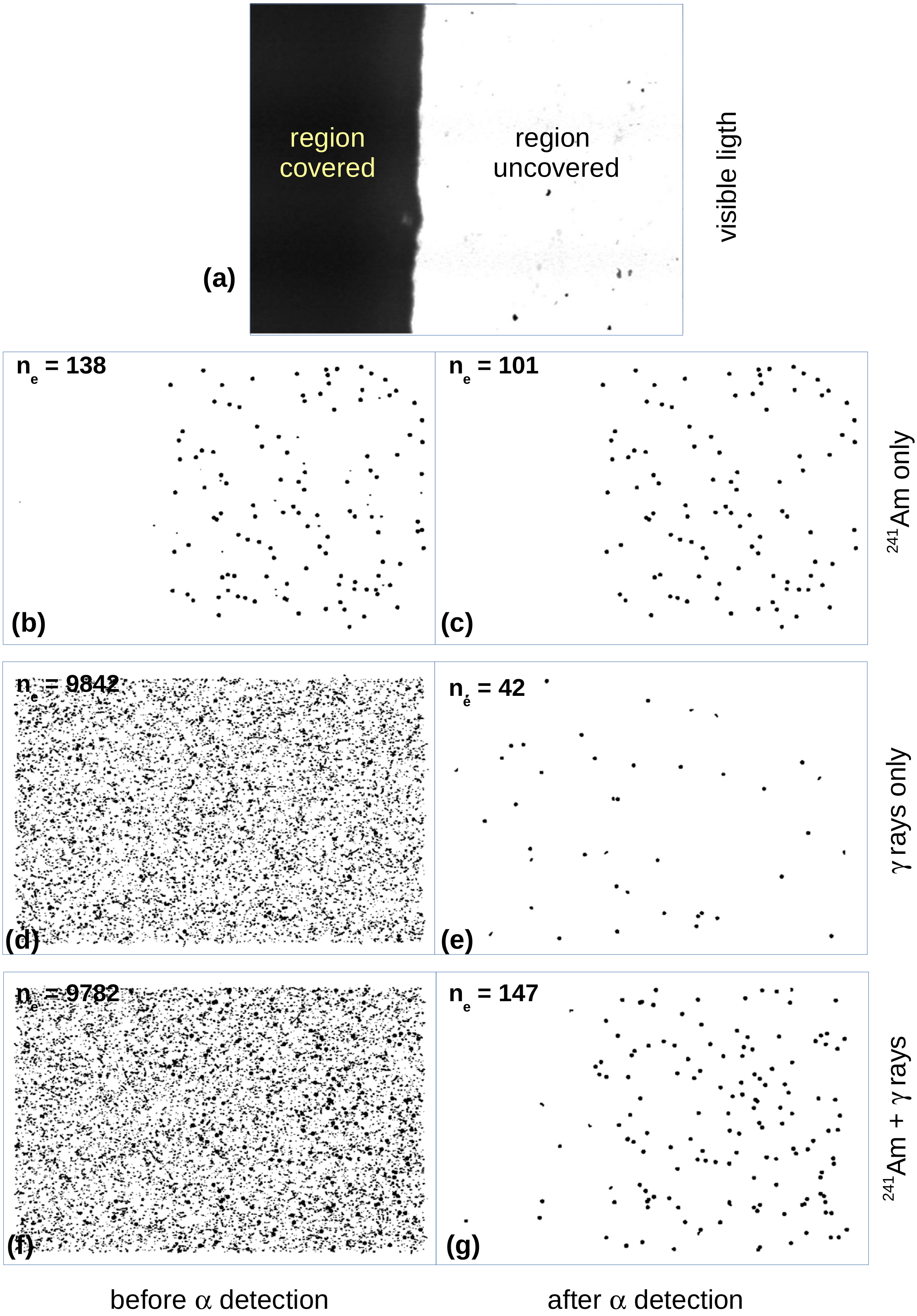

Fig. 12. Images obtained in order to analyze the method implemented to differentiate alpha and gamma particles. See details of each image in the text.

and conditions, complement previous results obtained in references [11–13], and [14]. These results show that with proper care and signal processing it is possible to use in several applications COTS CMOS image sensors as particle detectors. No total ionizing dose effects are analysed in this work, assuming that low doses are involved in the measurements.

Future work will be oriented to develop a stand-alone dosimetry system based on a similar image sensor, study the response to ions with known energies in a linear accelerator, and evaluate the use of new coatings as neutron converters.

Acknowledgments

This work was done under Grants PICT ANPCyT 2012-0770, PICT 2014-1969 and PIP CONICET 2011-0552. The authors would like to thank to Julio Marín, Eduardo Scarnicchia, and the staff of RA6 for the access to the reactor. Also to Leandro Tozzi and the INTI for his help with SEM and FIB measurements.

References

[1] Y. Degerli, F. Guilloux, F. Orsini, A novel CMOS sensor with in-pixel auto-zeroed discrimination for charged particle tracking, J. Instrum. 9 (05) (2014) C05018.

[2] F. Morel, C. Hu-Guo, G. Bertolone, G. Claus, C. Colledani, A. Dorokhov, G. Dozière, W. Dulinski, X. Fang, M. Goffe, et al., Mistral & astral: two cmos pixel sensor architectures suited to the inner tracking system of the alice experiment, J. Instrum. 9 (01) (2014) C01026.

[3] M. Mager, A. Collaboration, et al., Alpide, the monolithic active pixel sensor for the alice its upgrade, Nucl. Instrum. Methods Phys. Res. Sect. A: Accel. Spectrom. Detect. Assoc. Equip, http://dx.doi.org/10.1016/j.nima.2015.09.057.

[4] X. Llopart, M. Campbell, R. Dinapoli, D. San Segundo, E. Pernigotti, Medipix2: a 64-k pixel readout chip with 55-μsquare elements working in single photon counting mode, IEEE Trans. Nucl. Sci. 49 (5) (2002) 2279–2283.

[5] I. Perić, C. Kreidl, P. Fischer, Particle pixel detectors in high-voltage CMOS technology—new achievements, Nucl. Instrum. Methods Phys. Res. Sect. A: Accel. Spectrom. Detect. Assoc. Equip* 650 (1) (2011) 158–162.

[6] R. Turchetta, J. Berst, B. Casadei, G. Claus, C. Colledani, W. Dulinski, Y. Hu, D. Husson, J. Le Normand, J. Riester, et al., A monolithic active pixel sensor for charged particle tracking and imaging using standard VLSI CMOS technology, Nucl. Instrum. Methods Phys. Res. Sect. A: Accel. Spectrom. Detect. Assoc. Equip. 458 (3) (2001) 677–689.

[7] Y. Zhang, C. Hu-Guo, D. Husson, S. Higueret, T.-D. Lê, Y. Hu, Design of a monolithic CMOS sensor for high efficiency neutron counting, Microelectron. J. 43 (11) (2012) 730–736.

[8] M. Vanstalle, D. Husson, S. Higueret, M. Trocmé, T. Lê, A. Nourreddine, Demonstrating the γ-transparency of a CMOS pixel detector for a future neutron dosimeter, Nucl. Instrum. Methods Phys. Res. Sect. A: Accel. Spectrom. Detect. Assoc. Equip. 662 (1) (2012) 45–48.

[9] M. Vanstalle, D. Husson, S. Higueret, T. Le, A.-M. Nourreddine, Detection of thermal neutrons with a CMOS pixel sensor for a future dosemeter, IEEE Trans. Nucl. Sci. 59 (4) (2012) 1443–1447.

[10] J. Jerónimo Blostein, J. Estrada, A. Tartaglione, M. Sofo Haro, G. Fernández Moroni, G. Cancelo, Development of a novel neutron detection technique by using a boron layer coating a Charge Coupled Device, J. Instrum. 10 (2012) P01006 arXiv:1408.3263. URL http://dx.doi.org/10.1088/1748-0221/10/01/P01006.

[11] L. Servoli, D. Biagetti, D. Passeri, E.S. Gattuso, Characterization of standard CMOS pixel imagers as ionizing radiation detectors, J. Instrum. 5 (07) (2010) P07003.

[12] M. Paolucci, D. Battisti, M. Biasini, B. Checcucci, R. Di Lorenzo, A. Esposito, L. Fanò, D. Passeri, P. Placidi, L. Servoli, A real time active pixel dosimeter for interventional radiology, Radiat. Meas. 46 (11) (2011) 1271–1276.

[13] E. Conti, P. Placidi, M. Biasini, L. Bissi, A. Calandra, B. Checcucci, S. Chiocchini, R. Cicioni, R. Di Lorenzo, A.C. Dipilato, et al., Use of a CMOS image sensor for an active personal dosimeter in interventional radiology, IEEE Trans. Instrum. Meas. 62 (5) (2013) 1065–1072.

[14] S. Meroli, D. Biagetti, D. Passeri, P. Placidi, L. Servoli, P. Tucceri, A grazing angle technique to measure the charge collection efficiency for CMOS active pixel sensors, Nucl. Instrum. Methods Phys. Res. Sect. A: Accel. Spectrom. Detect. Assoc. Equip. 650 (1) (2011) 230–234.

[15] D. Whiteson, M. Mulhearn, C. Shimmin, K. Brodie, D. Burns, Observing ultra-high energy cosmic rays with smartphones, arXiv preprint arXiv:1410.2895, 2014.

[16] A. Karapetian, R. Some, J. Beahan, Radiation fault modeling and fault rate estimation for a cots based space-borne supercomputer, in: Aerospace Conference Proceedings, Big Sky, MT, USA, 5, IEEE, 2002, pp. 5-2121–5-2131. http://dx.doi.org/10.1109/AERO.2002.1035378.

[17] J.M. Lauenstein, Standards for Radiation Effects Testing: Ensuring Scientific Rigor in the Face of Budget Realities and Modern Device Challenges. URL ⟨http://www.ntrs.nasa.gov/search.jsp?R=20150011462⟩, 2015, (accessed October, 2015).

[18] R. Velazco, J. Clemente, G. Hubert, W. Mansour, C. Palomar, F. Franco, M. Baylac, S. Rey, O. Rosetto, F. Villa, Evidence of the robustness of a COTS soft-error free sram to neutron radiation, IEEE Trans. Nucl. Sci. 61 (6) (2014) 3103–3108, http://dx.doi.org/10.1109/TNS.2014.2363899.

[19] E. Martin, O. Gilard, T. Nuns, J. David, C. Virmontois, Prediction of CMOS image sensor dark current distribution and noise in a space radiation environment, IEEE Trans. Nucl. Sci. 60 (3) (2013) 2280–2287, http://dx.doi.org/10.1109/TNS.2013.2258938.

[20] R. Germanicus, S. Barde, L. Dusseau, G. Rolland, C. Barillot, F. Saigne, R. Ecoffet, P. Calvel, J. Fesquet, J. Gasiot, Evaluation and prediction of the degradation of a COTS CCD induced by displacement damage, IEEE Trans. Nucl. Sci. 49 (6) (2002) 2830–2835, http://dx.doi.org/10.1109/TNS.2002.805554.

[21] E. Martin, T. Nuns, C. Virmontois, J.-P. David, O. Gilard, Proton and gamma-rays irradiation-induced dark current random telegraph signal in a 0.18-μm CMOS image sensor, IEEE Trans. Nucl. Sci. 60 (4) (2013) 2503–2510, http://dx.doi.org/10.1109/TNS.2013.2251662.

[22] M. Perez, M.S. Haro, I. Sidelnik, L. Tozzi, D.R. Brito, C. Mora, J.J. Blostein, M.G. Berisso, J. Lipovetzky, Commercial CMOS pixel array for beta and gamma radiation particle counting, in: 2015 Argentine School of Micro-Nanoelectronics, Technology and Applications (EAMTA), 2015, pp. 11–16. http://dx.doi.org/10.1109/EAMTA.2015.7237371.

[23] C. Amsler, M. Doser, M. Antonelli, D. Asner, K. Babu, H. Baer, H. Band, R. Barnett, E. Bergren, J. Beringer, et al., Review of particle physics, Phys. Lett. B 667 (1) (2008) 1–6.

[24] J.H. Hubbell, N.I.O.S.S.M. Seltzer, Technology, Tables of X-ray Mass Attenuation Coefficients and Mass Energy-absorption Coefficients from 1 keV to 20 meV for elements $z=1$ to 92 and 48 Additional Substances of Dosimetric Interest, 1996, ⟨http://www.nist.gov/pml/data/xraycoef/⟩.

[25] M.Z.M.J. Berger, J.S. Coursey, J. Chang, Stopping-Power and Range Tables for Electrons, Protons, and Helium Ions, 2005.

[26] A. Holmes-Siedle, L. Adams, Handbook of Radiation Effects, Oxford Univ. Press, Inc., New York, NY, United States, 1993.

[27] L. Edmonds, Charge collection from ion tracks in simple epi diodes, IEEE Trans. Nucl. Sci. 44 (3) (1997) 1448–1463, http://dx.doi.org/10.1109/23.589631.

[28] B.L. Henke, E.M. Gullikson, J.C. Davis, X-ray interactions: photoabsorption, scattering, transmission, and reflection at $e=50$–30,000 eV, $z=1$–92, At. Data Nucl. Data Tables 54 (2) (1993) 181–342.

[29] I. Shcherback, O. Yadid-Pecht, CMOS APS crosstalk characterization via a unique submicron scanning system, IEEE Trans. Electron Dev. 50 (9) (2003) 1994–1997.

[30] I. Shcherback, T. Danov, O. Yadid-Pecht, A comprehensive CMOS APS crosstalk study: photoresponse model, technology, and design trends, IEEE Trans. Electron Dev. 51 (12) (2004) 2033–2041.

[31] H. Mutoh, 3-D optical and electrical simulation for CMOS image sensors, IEEE Trans. Electron Dev. 50 (1) (2003) 19–25.

[32] J. Estrada, J. Molina, J. Blostein, G. Fernandez, Plasma effect in silicon charge coupled devices (CCDs), Nucl. Instrum. Methods Phys. Res. Sect. A: Accel. Spectrom. Detect. Assoc. Equip. 665 (2011) 90–93.

[33] M.J. Ardito Batista, Estudio de dispositivos almacenadores de hidrógeno con la técnica de neutrografía (Ph.D. thesis), Universidad Nacional de Cuyo, 2013.

[34] A. Aguilar-Arevalo, D. Amidei, X. Bertou, D. Bole, M. Butner, G. Cancelo, A.C. Vázquez, A. Chavarria, J. Neto, S. Dixon, et al., Measurement of radioactive contamination in the high-resistivity silicon CCDs of the dynamic experiment, 2015, arXiv preprint arXiv:1506.02562.